ICAS-88-4.10.2

# THREE DIMENSIONAL FLOW SIMULATION WITH APPLICATION TO AEROELASTIC ANALYSIS

João Luiz F. Azevedo*
Instituto de Atividades Espaciais
São José dos Campos, S.P., Brasil

## Abstract

*The three dimensional flowfield about realistic launch vehicle configurations is simulated using the Reynolds-Averaged Navier-Stokes equations. Turbulent mixing is accounted for by means of the two-layer Baldwin and Lomax algebraic eddy viscosity model. The Beam and Warming implicit approximate factorization algorithm is used for the solution of the finite difference equations. Applications include the study of the flowfield about a hemisphere-cylinder configuration both in the subsonic and supersonic flight regimes, and about two hammerhead payload configurations at transonic speeds. Steady state results compare well with available experimental data or with theoretical results calculated by other schemes. A method is also described which permits incorporating this flow solver into a complete algorithm to perform time-domain aeroelastic stability analyses. The vehicle is modeled as a free-free beam and modal superposition techniques are used for the structural-dynamic formulation. Aeroelastic analyses were performed for the hammerhead configurations. The results showed good qualitative agreement with flight observations in the cases which these were available.*

## Nomenclature

| | |
|---|---|
| $a_\infty$ | freestream speed of sound |
| $\hat{A}, \hat{B}, \hat{C}$ | inviscid part of the flux Jacobian matrices |
| $C_p$ | specific heat at constant pressure |
| $Cp$ | pressure coefficient, $\frac{2}{\gamma M_\infty^2}\left(\frac{p}{p_\infty}-1\right)$ |
| $e$ | total energy per unit of volume |
| $\overline{E}, \overline{F}, \overline{G}$ | flux vectors |
| $I$ | identity matrix |
| $J$ | Jacobian of the transformation |
| $\ell_0$ | reference length |
| $\ell_b$ | dimensionless body length |
| $\ell(x,t)$ | dimensionless running normal force |
| $L_\xi, L_\eta, L_\zeta$ | left-hand side finite difference operators |
| $m(x)$ | mass per unit of body length |
| $\overline{m}_i$ | dimensionless generalized mass of the $i$-th mode |
| $M_\infty$ | freestream Mach number, $\frac{u_\infty}{a_\infty}$ |
| $\hat{M}_\xi, \hat{M}_\eta, \hat{M}_\zeta$ | viscous part of the flux Jacobian matrices |
| $N$ | number of modes used in the analysis |
| $p$ | pressure |
| $p_\infty$ | freestream pressure |
| $P_i(t)$ | generalized aerodynamic force |
| $Pr$ | Prandtl number |
| $Pr_t$ | turbulent Prandtl number |
| $q_i(t)$ | $i$-th generalized modal coordinate |
| $q_{x_i}$ | cartesian components of the heat flux vector |
| $\overline{Q}$ | vector of conserved quantities |
| $Re$ | Reynolds number |
| $R_\xi, R_\eta, R_\zeta$ | right-hand side finite difference operators |
| $t$ | time |
| $\Delta t$ | computational time step |
| $T$ | temperature |
| $u, v, w$ | cartesian components of fluid velocity |
| $U, V, W$ | contravariant velocity components |
| $u_\infty$ | magnitude of the freestream velocity vector |
| $x, y, z$ | cartesian coordinates |
| $\alpha$ | angle of attack |
| $\beta_x, \beta_y, \beta_z$ | terms defined in Equation 11 |
| $\gamma$ | ratio of specific heats |
| $\delta_{ij}$ | Kronecker delta |
| $\delta(x,t)$ | total deflection of the centerline |
| $\delta_\xi, \delta_\eta, \delta_\zeta$ | central difference operators |
| $\overline{\delta}_\xi, \overline{\delta}_\eta, \overline{\delta}_\zeta$ | midpoint central difference operators |
| $\Delta_\xi, \Delta_\eta, \Delta_\zeta, \Delta_t$ | forward difference operators |
| $\nabla_\xi, \nabla_\eta, \nabla_\zeta$ | backward difference operators |
| $\epsilon_E$ | artificial dissipation coefficient for explicit side |
| $\epsilon_I$ | artificial dissipation coefficient for implicit side |
| $\zeta_i$ | modal damping coefficient for the $i$-th mode |
| $\kappa$ | coefficient of thermal conductivity |
| $\kappa_\ell$ | laminar coefficient of thermal conductivity |
| $\kappa_t$ | eddy coefficient of thermal conductivity |
| $\mu$ | viscosity coefficient; effective viscosity coefficient |
| $\mu_\infty$ | freestream viscosity coefficient |
| $\mu_\ell$ | molecular (laminar) viscosity coefficient |
| $\mu_t$ | eddy (turbulent) viscosity coefficient |
| $\xi, \eta, \zeta$ | body-conforming coordinates |
| $\rho$ | density |
| $\rho_\infty$ | freestream density |
| $\tau$ | time in the body-conforming system |
| $\tau_{x_i x_j}$ | components of the viscous stress tensor |
| $\phi_i(x)$ | $i$-th normal mode of vibration |
| $\omega_i$ | natural frequency of the $i$-th mode |
| $\overline{\omega}_i$ | dimensionless frequency of the $i$-th mode |

## Introduction

Computational fluid dynamics (CFD) methods have shown a remarkable development over the recent years. Such progress has permitted the simulation of aerodynamic flowfields about realistic flight vehicle configurations. The present work uses this CFD technology to study the transonic flow, both steady and unsteady, about some launch vehicle configurations with particular interest in the so-called hammerhead payloads. Hemisphere-cylinder configurations are also considered at subsonic and low supersonic speeds in order to help ascertain the capabilities of the method.

The flow solver algorithm can be coupled to a structural-dynamic representation of the vehicle in order to perform aeroelastic stability analyses. In this case, the two sets of equations are integrated simultaneously in time, after an initial perturbation, in order to determine the aeroelastic stability of the given configuration. The present approach has the advantage that the aerodynamic nonlinearities present in the transonic regime can be captured by the method provided that the appropriate flow equations are used. This is in contrast with the classical methods for aeroelastic analysis in the transonic regime which usually have to rely on experimental data for the aerodynamic forces.

The present work will concentrate its efforts, however, in the aerodynamic simulation. The aeroelastic applications are mainly intended at demonstrating a very practical use of the methodology developed. Attention will be focused on the difficulties encountered in the computation of such complex flowfields. A detailed description of the numerical algorithm will be given with the objective of helping the understanding of the computational requirements of the method, both in terms of storage as well as processing time.

The theoretical formulation will be presented next, followed by a detailed discussion of the numerical implementation of the method. The first examples will concern a hemisphere-cylinder configuration. The flow about this configuration at different values of Mach number will be studied and the resulting steady solutions discussed. Afterwards, two hammerhead payload configurations will be considered. Both steady state and aeroelastic results will be presented and discussed. Finally,

*Assistant Research Engineer, Design Division

considerations about the current status of the method and the perspectives for future developments will be made.

## Theoretical Formulation

### Aerodynamic Problem

The correct simulation of the flowfields we are concerned with in the present work dictates that a Navier-Stokes formulation should be used. Current computational capabilities, however, prevent the full solution of these equations. Therefore, the method presented here undertakes to solve the Reynolds-Averaged Navier-Stokes equations [1,2]. These equations can be written in strong conservation-law form [3] for general three dimensional, body-conforming, curvilinear coordinates as

$$\frac{\partial \overline{Q}}{\partial \tau} + \frac{\partial \overline{E}}{\partial \xi} + \frac{\partial \overline{F}}{\partial \eta} + \frac{\partial \overline{G}}{\partial \zeta} = 0 \tag{1}$$

The curvilinear coordinate system is defined such that $\xi$ is the longitudinal direction, $\eta$ is the normal direction, and $\zeta$ is the circumferential direction. The transformation of variables is given by

$$\begin{aligned} \tau &= t \\ \xi &= \xi(x,y,z,t) \\ \eta &= \eta(x,y,z,t) \\ \zeta &= \zeta(x,y,z,t) \end{aligned} \tag{2}$$

The vector of conserved quantities, $\overline{Q}$, is defined as

$$\overline{Q} = J^{-1} \begin{Bmatrix} \rho \\ \rho u \\ \rho v \\ \rho w \\ e \end{Bmatrix} \tag{3}$$

where the Jacobian of the transformation can be expressed as

$$J = \left(x_\xi y_\eta z_\zeta + x_\eta y_\zeta z_\xi + x_\zeta y_\xi z_\eta - x_\xi y_\zeta z_\eta - x_\eta y_\xi z_\zeta - x_\zeta y_\eta z_\xi\right)^{-1} \tag{4}$$

The flux vectors $\overline{E}$, $\overline{F}$ and $\overline{G}$ can be written as

$$\overline{E} = J^{-1} \begin{Bmatrix} \rho U \\ \rho u U + p\xi_x - \frac{M_\infty}{Re}\left(\tau_{xx}\xi_x + \tau_{xy}\xi_y + \tau_{xz}\xi_z\right) \\ \rho v U + p\xi_y - \frac{M_\infty}{Re}\left(\tau_{xy}\xi_x + \tau_{yy}\xi_y + \tau_{yz}\xi_z\right) \\ \rho w U + p\xi_z - \frac{M_\infty}{Re}\left(\tau_{xz}\xi_x + \tau_{yz}\xi_y + \tau_{zz}\xi_z\right) \\ (e+p)U - p\xi_t - \frac{M_\infty}{Re}\left(\beta_x\xi_x + \beta_y\xi_y + \beta_z\xi_z\right) \end{Bmatrix} \tag{5}$$

$$\overline{F} = J^{-1} \begin{Bmatrix} \rho V \\ \rho u V + p\eta_x - \frac{M_\infty}{Re}\left(\tau_{xx}\eta_x + \tau_{xy}\eta_y + \tau_{xz}\eta_z\right) \\ \rho v V + p\eta_y - \frac{M_\infty}{Re}\left(\tau_{xy}\eta_x + \tau_{yy}\eta_y + \tau_{yz}\eta_z\right) \\ \rho w V + p\eta_z - \frac{M_\infty}{Re}\left(\tau_{xz}\eta_x + \tau_{yz}\eta_y + \tau_{zz}\eta_z\right) \\ (e+p)V - p\eta_t - \frac{M_\infty}{Re}\left(\beta_x\eta_x + \beta_y\eta_y + \beta_z\eta_z\right) \end{Bmatrix} \tag{6}$$

$$\overline{G} = J^{-1} \begin{Bmatrix} \rho W \\ \rho u W + p\zeta_x - \frac{M_\infty}{Re}\left(\tau_{xx}\zeta_x + \tau_{xy}\zeta_y + \tau_{xz}\zeta_z\right) \\ \rho v W + p\zeta_y - \frac{M_\infty}{Re}\left(\tau_{xy}\zeta_x + \tau_{yy}\zeta_y + \tau_{yz}\zeta_z\right) \\ \rho w W + p\zeta_z - \frac{M_\infty}{Re}\left(\tau_{xz}\zeta_x + \tau_{yz}\zeta_y + \tau_{zz}\zeta_z\right) \\ (e+p)W - p\zeta_t - \frac{M_\infty}{Re}\left(\beta_x\zeta_x + \beta_y\zeta_y + \beta_z\zeta_z\right) \end{Bmatrix} \tag{7}$$

The equations have been nondimensionalized following the work of Pulliam and Steger [4]. The density $\rho$ is referred to the freestream density $\rho_\infty$, the cartesian velocity components are made dimensionless with respect to the freestream speed of sound $a_\infty$, and the total energy per unit of volume $e$ is referenced to $\rho_\infty a_\infty^2$. The Reynolds number is defined in its usual way as

$$Re = \frac{\rho_\infty U_\infty \ell_0}{\mu_\infty} \tag{8}$$

The pressure is calculated by the equation of state for perfect gases and, therefore, can be obtained as

$$p = (\gamma - 1)\left[e - \frac{1}{2}\rho\left(u^2 + v^2 + w^2\right)\right] \tag{9}$$

The contravariant velocity components are defined as

$$\begin{aligned} U &= \xi_t + \xi_x u + \xi_y v + \xi_z w \\ V &= \eta_t + \eta_x u + \eta_y v + \eta_z w \\ W &= \zeta_t + \zeta_x u + \zeta_y v + \zeta_z w \end{aligned} \tag{10}$$

The $\beta_x$, $\beta_y$ and $\beta_z$ terms are given by

$$\begin{aligned} \beta_x &= \tau_{xx}u + \tau_{xy}v + \tau_{xz}w - q_x \\ \beta_y &= \tau_{xy}u + \tau_{yy}v + \tau_{yz}w - q_y \\ \beta_z &= \tau_{xz}u + \tau_{yz}v + \tau_{zz}w - q_z \end{aligned} \tag{11}$$

The components of the viscous stress tensor can be written

$$\tau_{x_i x_j} = \mu\left(\frac{\partial u_i}{\partial x_j} + \frac{\partial u_j}{\partial x_i}\right) - \frac{2}{3}\mu\left(\frac{\partial u_k}{\partial x_k}\right)\delta_{ij} \tag{12}$$

where we are considering an isotropic fluid and that the second coefficient of viscosity $\lambda$ is given by: $\lambda = -\frac{2}{3}\mu$. In the interest of brevity, we have used the index notation in Equation 12, and we are also assuming the Einstein convention with the repeated-index implying summation. Still using the same notation, we can write the components of the heat-flux vector as

$$q_{x_j} = -\kappa\frac{\partial T}{\partial x_j} \tag{13}$$

Finally, the metric relations can be expressed as

$$\begin{aligned} \xi_x &= J\left(y_\eta z_\zeta - y_\zeta z_\eta\right) & \xi_y &= J\left(x_\zeta z_\eta - x_\eta z_\zeta\right) \\ \zeta_x &= J\left(x_\eta y_\zeta - x_\zeta y_\eta\right) & \xi_t &= -x_\tau\xi_x - y_\tau\xi_y - z_\tau\xi_z \\ \eta_x &= J\left(y_\zeta z_\xi - y_\xi z_\zeta\right) & \eta_y &= J\left(x_\xi z_\zeta - x_\zeta z_\xi\right) \\ \eta_z &= J\left(x_\zeta y_\xi - x_\xi y_\zeta\right) & \eta_t &= -x_\tau\eta_x - y_\tau\eta_y - z_\tau\eta_z \\ \zeta_x &= J\left(y_\xi z_\eta - y_\eta z_\xi\right) & \zeta_y &= J\left(x_\eta z_\xi - x_\xi z_\eta\right) \\ \zeta_z &= J\left(x_\xi y_\eta - x_\eta y_\xi\right) & \zeta_t &= -x_\tau\zeta_x - y_\tau\zeta_y - z_\tau\zeta_z \end{aligned} \tag{14}$$

The Boussinesq concept of *effective viscosity* [5] is used to model the Reynolds stress terms and turbulent heat flux terms that appear in the time-averaging of the equations. By this approach, the turbulent mixing processes are accounted for by *eddy viscosity* and *eddy conductivity* coefficients. The viscosity coefficient that appears in the definition of the viscous stress terms is formed as

$$\mu \leftarrow \mu_\ell + \mu_t \tag{15}$$

Similarly, the coefficient of thermal conductivity can be obtained as

$$\kappa \leftarrow \kappa_\ell + \kappa_t = \frac{C_p\mu_\ell}{Pr} + \frac{C_p\mu_t}{Pr_t} \tag{16}$$

The two-layer Baldwin and Lomax [6] algebraic eddy viscosity model is used in the present work to determine $\mu_t$. The model is implemented such that

$$\mu_t = \begin{cases} (\mu_t)_{\text{inner}} & , \eta \le \eta_{\text{crossover}} \\ (\mu_t)_{\text{outer}} & , \eta > \eta_{\text{crossover}} \end{cases} \tag{17}$$

The inner region uses a Prandtl-Van Driest formulation, and the expression for the outer region is similar to a Clauser formulation. As throughout this work, $\eta$ is the distance normal to the wall and $\eta_{\text{crossover}}$ is the smallest value of $\eta$ at which the inner and outer formulations give equal values.

### Aeroelastic Problem

The aeroelastic formulation is obtained by coupling the previously described flow solver equations with appropriate structural-dynamic equations for the vehicle. The latter are developed considering that the vehicle can be modelled as a free-free beam in flexural vibration. This equivalent beam is allowed to have variable properties, but we assume that the motion is restricted to the pitch plane. Moreover, a modal superposition technique is used, and we assume that a set of normal modes of free vibration is known for the vehicle.

Hence, the total deflection at any station along the body can be obtained as

$$\delta(x,t) = \sum_{i=1}^{N} q_i(t)\,\phi_i(x) \tag{18}$$

To be consistent with the aerodynamic formulation, $\delta(x,t)$ and $q_i(t)$ have been nondimensionalized with respect to the reference length $\ell_0$

used for the aerodynamic equations. The equation of motion for each of the $i$-th coordinates ($i = 1, \ldots, N$) can be written as

$$\overline{m}_i \left[\ddot{q}_i(t) + 2\zeta_i \overline{\omega}_i \dot{q}_i(t) + \overline{\omega}_i^2 q_i(t)\right] = P_i(t) \tag{19}$$

Here again the quantities have already been made dimensionless, and the dots indicate derivatives with respect to nondimensional time. The dimensionless natural frequencies are defined by

$$\overline{\omega}_i = \frac{\ell_0 \omega_i}{a_\infty} \tag{20}$$

The dimensionless generalized masses are calculated from

$$\overline{m}_i = \int_0^{\ell_b} \frac{m(x)}{\rho_\infty \ell_0^2} \left|\phi_i(x)\right|^2 dx \tag{21}$$

Finally, the generalized aerodynamic forces can be obtained from

$$P_i(t) = \int_0^{\ell_b} \ell(x,t)\phi_i(x) dx \tag{22}$$

The reader should note that $P_i(t)$ is being called *generalized aerodynamic force* just to keep some resemblance in nomenclature with classical aeroelastic analysis by means of modal superposition. The character of $P_i(t)$ is, however, quite different. Although associated with the $i$-th mode, $P_i(t)$ actually has contributions from all the modes through the running normal force. The latter is obtained from the pressure distribution calculated in the numerical solution of the Navier-Stokes equations. Therefore, the actual contribution of the present work is associated with the use of the aerodynamic forcing term in such fashion. This permits capturing the aerodynamic nonlinearities present in the transonic regime, while still keeping a fairly simple structural-dynamic formulation.

The procedure for solving the complete aeroelastic problem consists in the simultaneous time integration of the two sets of equations, i. e. , Equation 1 describing the flow behavior and Equation 19 for the structural-dynamic representation of the vehicle. The solution of the aerodynamic equations gives the forcing terms for the aeroelastic analysis. Solution of the structural-dynamic equations provides the new deformed shape of the body and the boundary conditions for the aerodynamic equations in the next time step. Time-domain analyses are performed which allow the study of the aeroelastic stability at each particular flight condition. Following the response of the vehicle to an initial perturbation, we can determine whether the configuration is stable or unstable. Since the problem is nonlinear, the response should be monitored over several cycles of the lowest mode considered before a conclusion could be reached regarding the stability of the vehicle.

## Implementation of the Method

The equations previously described were implemented using finite difference methods. The flow solver implementation received more attention because, in this case, it constitutes the more complex problem. There is a huge amount of data that has to be stored and processed. Therefore, a fair amount of optimization in the database structure and in the sequence of operations in the code is almost essential to allow for reasonable computational times. The code should also be structured in such a way that it permits large amounts of vectorization in order to take full advantage of the current generation of supercomputers now in use. These requirements become even more stringent when unsteady applications are involved.

We will initially consider the implementation of the aerodynamic equations. The spatial derivatives are approximated using three-point, second order central differencing, and the equations are advanced in time by means of the implicit Euler method. The Beam and Warming [7] implicit approximate factorization scheme is used for the solution of the finite difference equations. The algorithm is second order accurate in space, but only first order accurate in time [8] because the implicit Euler method was used. Due to the particular database structure implemented in the present code, it is advantageous to write the factored finite difference equations as

$$L_\eta L_\zeta L_\xi \Delta_t \overline{Q}^n = R_\xi + R_\eta + R_\zeta \tag{23}$$

The above operators are defined as

$$\begin{aligned}
L_\xi &= \left(I + \Delta t \delta_\xi \hat{A}^n - \epsilon_I \Delta t J^{-1} \nabla_\xi \Delta_\xi J - \Delta t M_\infty \mathrm{Re}^{-1} \overline{\delta_\xi} J^{-1} \hat{M}_\xi^n J\right) \\
L_\eta &= \left(I + \Delta t \delta_\eta \hat{B}^n - \epsilon_I \Delta t J^{-1} \nabla_\eta \Delta_\eta J - \Delta t M_\infty \mathrm{Re}^{-1} \overline{\delta_\eta} J^{-1} \hat{M}_\eta^n J\right) \\
L_\zeta &= \left(I + \Delta t \delta_\zeta \hat{C}^n - \epsilon_I \Delta t J^{-1} \nabla_\zeta \Delta_\zeta J - \Delta t M_\infty \mathrm{Re}^{-1} \overline{\delta_\zeta} J^{-1} \hat{M}_\zeta^n J\right) \\
R_\xi &= -\Delta t \delta_\xi \overline{E}^n - \epsilon_E \Delta t J^{-1} \left(\nabla_\xi \Delta_\xi\right)^2 J\overline{Q}^n \\
R_\eta &= -\Delta t \delta_\eta \overline{F}^n - \epsilon_E \Delta t J^{-1} \left(\nabla_\eta \Delta_\eta\right)^2 J\overline{Q}^n \\
R_\zeta &= -\Delta t \delta_\zeta \overline{G}^n - \epsilon_E \Delta t J^{-1} \left(\nabla_\zeta \Delta_\zeta\right)^2 J\overline{Q}^n
\end{aligned} \tag{24}$$

Here, artificial dissipation terms have been introduced in the operators in order to maintain the stability of the numerical solution process. The Jacobian matrices are described in detail in References [9] and [10].

The structural-dynamic equations are differenced using second order accurate formulas [11] to approximate the time derivatives. The finite difference equation that permits advancing in time each of the generalized modal coordinates can be written

$$q_{i,n+1} = \frac{\left[2 - (\Delta t)^2 \overline{\omega}_i^2\right] q_{i,n} - \left(1 - \Delta t \zeta_i \overline{\omega}_i\right) q_{i,n-1} + (\Delta t)^2 \frac{P_{i,n}}{\overline{m}_i}}{\left(1 + \Delta t \zeta_i \overline{\omega}_i\right)} \tag{25}$$

It must be emphasized that a set of scalar equations is obtained for the solution of the structural-dynamic problem because of the assumption that normal modes are known. If the modes were coupled, a matrix equation would be obtained. Nevertheless, since the number of modes that would typically be used in an aeroelastic analysis is extremely small when compared to the size of the matrices involved in the solution of the aerodynamic problem, it is clear that the solution for the $q_{i,n+1}$ is not the limiting step in the process.

The coupling of the two sets of equations is obtained by integrating them simultaneously in time and ensuring that the updated data generated by one set is used in the next solution of the other. At a given time step, the solution of the aerodynamic equations gives the pressure distribution on the body. Suitable circumferential integration of this pressure distribution yields the running normal force and, therefore, the generalized aerodynamic forces by means of Equation 22. These are used as forcing terms for the structural-dynamic equations in the current time step. On the other hand, solution of the latter provides the new deformed position of the body and the boundary conditions for the solution of the aerodynamic problem in the next time step. It must also be emphasized that to perform an aeroelastic analysis we are assuming that a steady state aerodynamic solution for the rigid vehicle was already obtained at the current flight condition. This will be used as initial condition for the aeroelastic problem.

The database is structured in a pencil format [12] with the objective of reducing the amount of data that has to be kept in core at a given time. Therefore, the majority of the data is kept in mass storage disk files. Only the specific portion (or *pencil*) being operated at the particular time is brought into the core. Extensive use of asynchronous I/O is made which improves the efficiency of the read/write operations. The code was optimized for a CDC Cyber 205 and it is highly vectorized. The sequence of operations in a typical time step for unsteady solution is described below in a schematic fashion.

1. Initialization:
   - Read: grid
   - Compute: metrics and Jacobian
   - Write: all metrics and Jacobian
2. x-direction:
   - Read: $\overline{Q}^n$, $J$ and $\xi$-metrics
   - Compute: $R_\xi$
   - Write: $R_\xi$
3. z-direction:
   - Read: $\overline{Q}^n$, $J$, $\zeta$-metrics and current residue
   - Compute: $R_\zeta$
   - Write: $(R_\xi + R_\zeta)$

4. y-direction:
   - Read: $\overline{Q}^n$, $J$, $\eta$-metrics and current residue
   - Compute: $R_\eta$, $L_\eta$ and solve it
   - Write: $L_\eta^{-1}\left(R_\xi + R_\eta + R_\zeta\right)$
5. z-direction:
   - Read: $\overline{Q}^n$, $J$, $\zeta$-metrics and current residue
   - Compute: $L_\zeta$ and solve it
   - Write: $L_\zeta^{-1}L_\eta^{-1}\left(R_\xi + R_\eta + R_\zeta\right)$
6. x-direction:
   - Read: $\overline{Q}^n$, $J$, $\xi$-metrics and current residue
   - Compute: $L_\xi$, $\Delta_t\overline{Q}^n$ and $\overline{Q}^{n+1}$
   - Write: $\overline{Q}^{n+1}$
7. Structural-dynamics:
   - Read: $\overline{Q}^{n+1}$ and $J$ (on the body only)
   - Compute: $P_{i,n}$ and $q_{i,n+1}$
8. New grid:
   - Read: old grid
   - Compute: new grid, new metrics and Jacobian
   - Write: metrics and Jacobian
9. $n \leftarrow n+1$ , and go back to step (2).

If a steady state aerodynamic case is being considered, the same algorithm can be used except that steps (7) and (8) are omitted. Furthermore, the calculation of $R_\xi$ can be done directly at the end of step (6) which saves a large number of read operations. In unsteady calculations, the grid velocities are obtained from first order accurate formulas which use the known grid positions at the previous and current iterations. The new Jacobian is saved in the disk files at the end of step (8), however the conserved quantities are not rescaled at this point in order to take into consideration the changes in the Jacobian. We let these variations be corrected by the next time step of the aerodynamic equations. The termination of the process is usually obtained by specifying the desired number of iterations.

## Hemisphere-Cylinder Cases

Due to the simplicity of the geometry, while still keeping the general launch vehicle shape, a hemisphere-cylinder configuration was chosen to test the code before going into the analysis of more complex problems. Such configuration is also attractive from the standpoint that experimental, or other computational results are available in the literature. The cases studied for this configuration include steady state calculations for freestream Mach numbers of 0.5 and 1.5, both cases at zero angle of attack. For the hemisphere-cylinder computations the turbulence model was turned off, such that these are laminar results.

The body conforming computational mesh was generated using algebraic methods, and the same mesh was used for all hemisphere-cylinder cases analyzed. Grid lines run in the longitudinal, normal and circumferential directions, and 50, 40 and 20 grid points were used, respectively, in each of these directions. This is a fairly coarse grid system, and it was used because it would allow for a faster turnaround time in these preliminary computations.

A general three dimensional view of body and grid can be seen in Figure 1. Mesh points in the normal direction are clustered near the body in order to capture viscous effects, and a 25% exponential grid stretching is used in this direction. Over the hemispherical part of the body, grid lines in the longitudinal direction are placed at equal angular increments, and over the cylindrical part of it, these lines are equally spaced. The 50 points used in the longitudinal direction are distributed such that 15 of them are over the hemispherical part of the body, and the other 35 points are located in the cylindrical section. Grid lines in the circumferential direction are generated by rotating one longitudinal plane at equally spaced angles around the body. Note

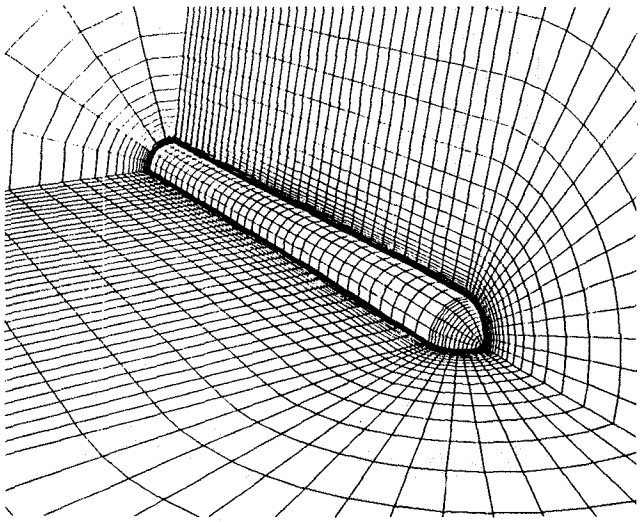

Figure 1: General three dimensional view of the hemisphere-cylinder grid.

that two circumferential planes are overlapped in order to facilitate the enforcement of the boundary conditions when operating in this direction.

As an initial test for the code, we started with a subsonic freestream case. It is clear that low subsonic cases should converge faster to a steady state, however one should be careful not to approach the incompressible limit. Essentially the problem is that we are using a compressible Navier-Stokes formulation, and the system of equations becomes numerically ill-behaved when the incompressible limit is approached. A case at $M_\infty = 0.5$ seemed to be a good compromise and it was considered for these initial computations. Later, one low supersonic case was run to verify the capabilities of the code for supersonic problems.

The first case run for the hemisphere-cylinder configuration was at a Mach number of 0.5, for zero angle of attack, and a Reynolds number of 1.5 million based on the cylindrical section diameter. Pressure coefficient contours for the converged steady state solution along two opposing longitudinal planes can be seen in Figure 2 . Mach contours are also shown in the same figure.

Since experimental results could not be found for this case in the literature, the present computations were compared to results obtained from another finite difference code, namely the F3D code [13,14]. The F3D computations were performed on a Cray 2 supercomputer, but the grid system was essentially the same used for the Cyber computations in order to make the two calculations comparable. Plots of the pressure coefficient distributions on the body for the two computations are presented in Figure 3 . As can be seen from this figure, the two computations show good agreement. The results from the F3D code show a *faster* expansion over the hemispherical part of the body, and also predict a slightly higher magnitude for the negative peak $Cp$ around the hemisphere-cylinder intersection. Both computations show this negative peak on the pressure coefficient occuring ahead of the hemisphere-cylinder intersection. The F3D results also seem to return faster to the freestream pressure value over the cylindrical section of the body. Also shown in Figure 3 is the value of the pressure coefficient at the nose stagnation point as predicted by isentropic relations [15]. These relations predict $Cp = 1.06$ at the stagnation point, and both calculations agree well with that value.

Computational results for a freestream Mach number $M_\infty = 1.5$ case can be seen in Figure 4. In this case the Reynolds number was 1.386 million, based on the reference diameter, and again zero angle of attack was considered. This value of Reynolds number was chosen to match the experimental results presented by Hsieh [16,17]. A plot of the bow shock location, calculated based on pressure gradient results, is shown in Figure 5 . It should be pointed out that in Figure 5($b$) we actually have a complete shock surface. It was plotted only as lines in order to let the body be also seen behind the shock. The shock standoff distance can be calculated as $-0.57$ , nondimensionalized with respect to the radius of the cylindrical section. This result compares well with the

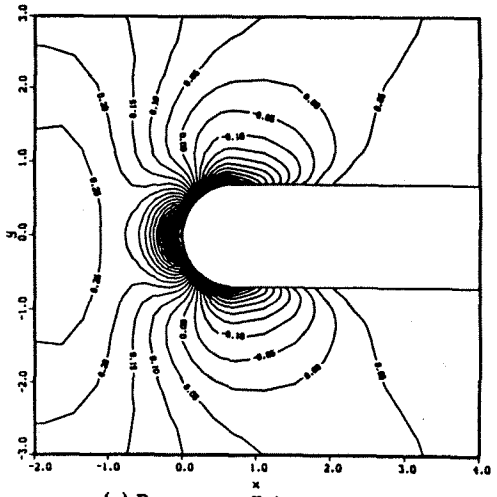

(*a*) Pressure coefficient contours.

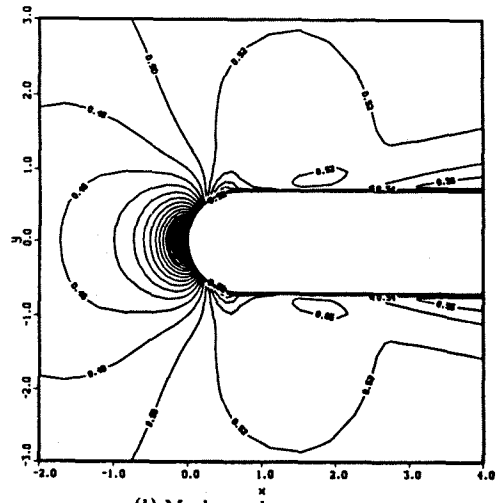

(*b*) Mach number contours.

Figure 2: Flow solution for hemisphere-cylinder at $M_\infty = 0.5$ and $\alpha = 0°$.

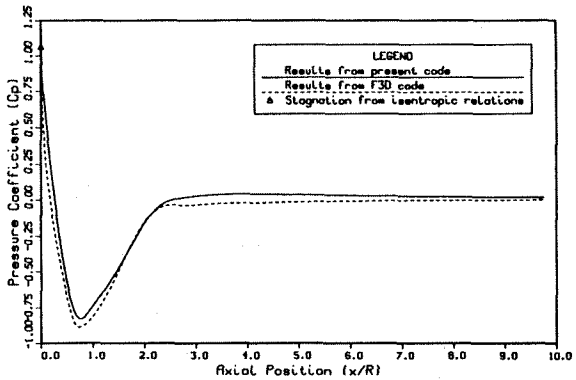


Figure 3: Pressure coefficient distribution on the body for hemisphere-cylinder at $M_\infty = 0.5$, $\alpha = 0°$, and $Re = 1.5 \times 10^6$.

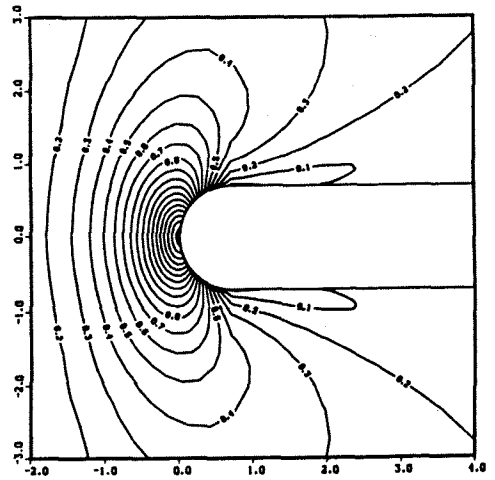

Figure 4: Pressure coefficient contours for hemisphere-cylinder at $M_\infty = 1.5$, $\alpha = 0°$, and $Re = 1.386 \times 10^6$.

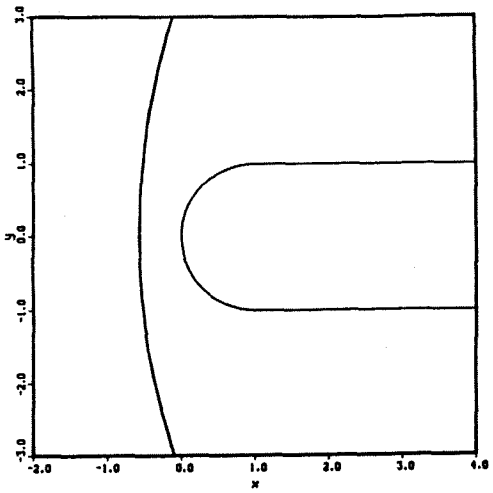

(*a*) 2-D view.

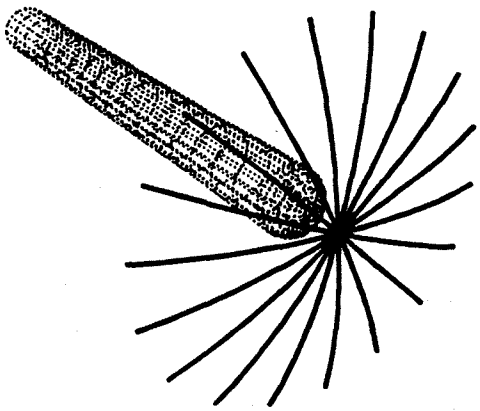

(*b*) 3-D view.

Figure 5: Shock location based on pressure gradient for hemisphere-cylinder at $M_\infty = 1.5$ and $\alpha = 0°$.

value of $-0.60$ for the shock standoff distance for a hemisphere-cylinder obtained from shadowgraphs, presented in Reference [16]. However, it is clear from Figure 4 that the computations are not capturing such a crisp, well-defined shock as Figure 5 may suggest. The most obvious reason for that is the coarseness of the grid.

Although the steady state cases shown above for the hemisphere-cylinder configuration cannot be considered extremely difficult problems for many existing computational fluid dynamics codes, these results provided confidence in the present code. It must be mentioned that both steady state and unsteady calculations were performed using the same configuration at $M_\infty = 0.6$ flight Mach number. These results are described in References [10] and [11]. The unsteady applications involved rigid body pitching of the vehicle, and the determination of the resulting unsteady airloads.

## Hammerhead Payload Cases

The first hammerhead configuration studied is shown in Figure 6. This figure also gives a three dimensional view of the computational grid used for this application. The mesh was generated by algebraic methods, and it has 105 x 66 x 38 points in the longitudinal, normal and circumferential directions, respectively. The grid is periodic in the circumferential direction. A 16% exponential grid stretching is used in the normal direction in order to cluster grid points near the body for capturing the viscous effects. One parameter hyperbolic tangent grid stretching is used in the longitudinal direction to concentrate points around the upstream centerline, and the hemisphere-forebody cylinder and the flare-afterbody cylinder intersections. A 8.5% exponential stretching is also used in the afterbody cylinder section with the objective of increasing the grid spacing towards the downstream boundary.

The steady state flow solution was calculated over this geometry for a freestream Mach number $M_\infty = 0.85$, an angle of attack $\alpha = 6°$, and the Reynolds number $Re = 1.26 \times 10^6$ (based on the "neck" diameter). The turbulence model was turned on, or in other words, these are turbulent computational results. Pressure coefficient contours and Mach number contours for leeside and windside are shown in Figure 7, where we are looking at a side view of the body. The expected flowfield features are reproduced by the computation. For instance, the expansion regions around the hemisphere-forebody cylinder intersection and around the flare-afterbody cylinder intersection are clearly shown in the figures. A mild expansion around the forebody cylinder-boattail intersection can be seen, and the compression region on the face of the flare, mainly on the windside, is also very well defined.

It should be clear that the amount of data generated in these three dimensional computational solutions is very large. The study of scalar flow variable contours may prove inadequate to understand what is really happening. To this end, particle traces are very useful. In particular, particle traces restricted to the first computational $\eta$-plane away from the body amount to computer generated *oil-flow* lines and are almost indispensable to understand the topology of the flow. It should be pointed out that the latter can also be interpreted as plots of the skin-friction lines on the body. We shall not go into any detailed discussion of these flow topologies, except to point out lines of separation and/or reattachment as those will help us understand the solutions that are being obtained. The reader interested on detailed discussions of topological flow structures is referred, for example, to the works of Dallmann [18,19], Kaynak, Holst and Cantwell [20], and Deiwert [21].

Figure 8 shows these computer generated oil-flow lines for this configuration at the converged steady state solution. One can clearly identify a separation region on the cylindrical forebody right after the hemisphere-cylinder intersection, and a node of separation can be seen on the lee generator just behind this intersection. There is another separation line on the boattail, which indicates that even the windside experiences some flow separation in that region. The line of reattachment aft of the boattail is also clearly defined in the figures. All those cases can be considered mild separations, in the sense that the regions of reversed flow are rather limited.

This steady state aerodynamic solution was used as the starting flow solution for the aeroelastic cases analyzed for this configuration. Since this solution was calculated for a rigid vehicle, the airloads are not the correct actual loads at a deformed equilibrium position for the elastic vehicle. This provides a way of introducing the *initial perturbation* to start the oscillation, which will be adopted in the present work for all cases where the freestream angle of attack is different from zero.

The procedure followed was to keep the flight Mach number and the angle of attack constants, and vary the dynamic pressure. The values of structural damping coefficient used were $\varsigma_1 = 0.0010$, $\varsigma_2 = 0.0018$ and $\varsigma_3 = 0.0036$, for the first, second and third modes, respectively. A typical vehicle response for an intermediate value of dynamic pressure for this case can be seen in Reference [11]. Several other runs, for different values of dynamic pressure, were performed for this configuration with the objective of determining its aeroelastic stability boundary at this flight condition. This configuration turned out to be always stable for flight at $M_\infty = 0.85$ and $\alpha = 6°$.

Despite the fact that the present method uses time domain analyses, the results are best summarized in a root locus plot, which is shown in Figure 9. In this plot the arrows indicate the direction of increasing dynamic pressure, which was the parameter varied in the analysis. The abscissa is the real part of the aeroelastic root, which is a measure of the rate of the decay of the oscillation in each mode, formed by the product

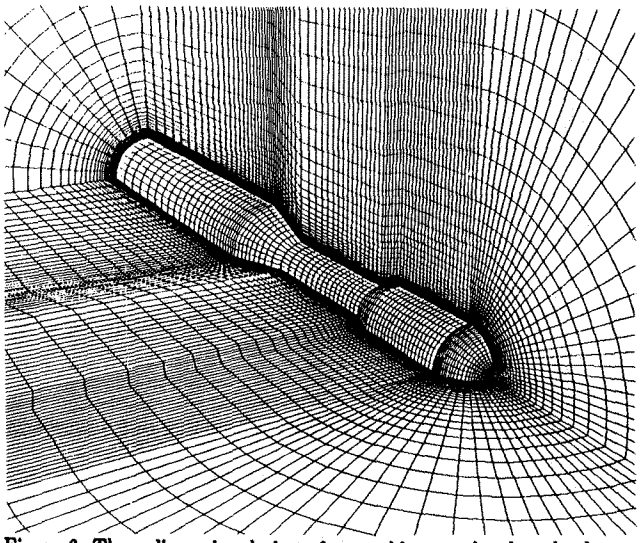

Figure 6: Three dimensional view of general hammerhead payload configuration grid system.

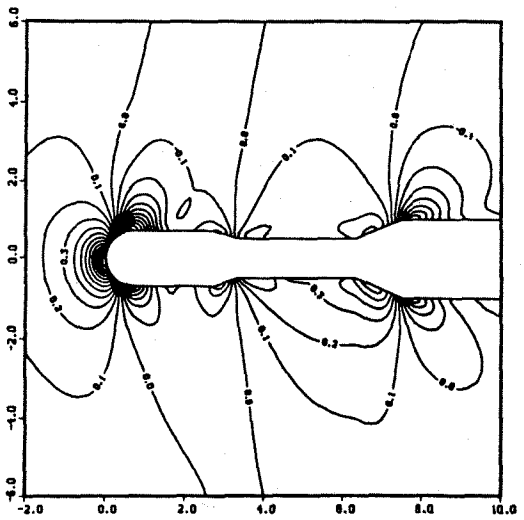

(*a*) Pressure coefficient contours.

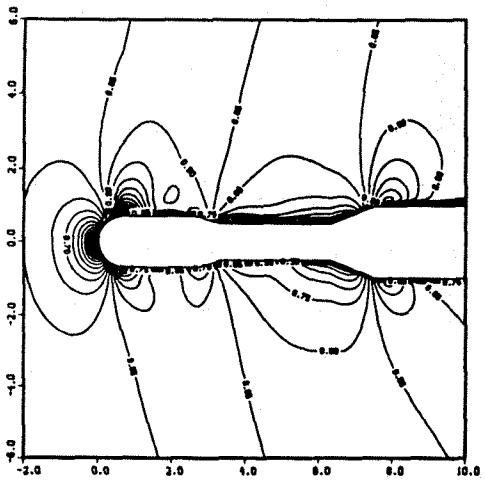

(*b*) Mach number contours.

Figure 7: Flow solution about a hammerhead geometry at $M_\infty = 0.85$, $\alpha = 6°$ and $Re = 1.26 \times 10^6$ (side view).

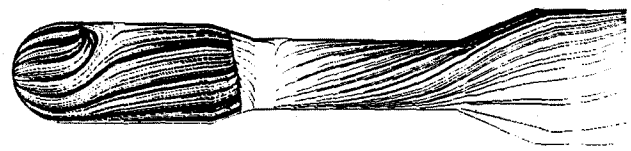

(*a*) Side view.

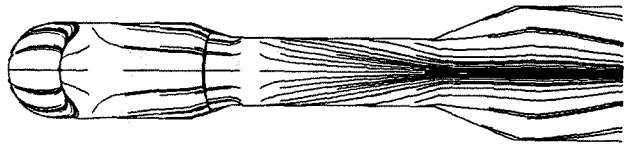

(*b*) Top view.

Figure 8: Computer generated oil-flow lines for general hammerhead payload at $M_\infty = 0.85$ and $\alpha = 6°$ .

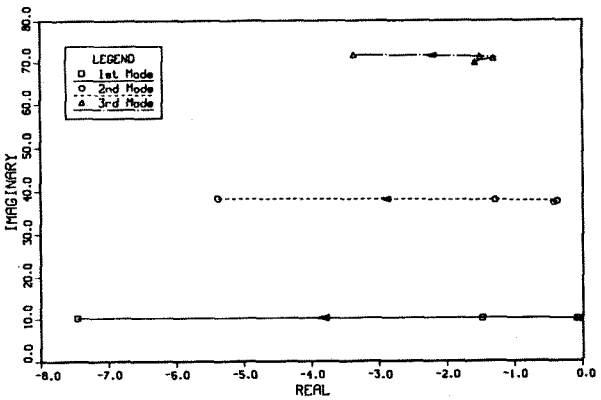


Figure 9: Aeroelatic root loci for general hammerhead configuration at $M_\infty = 0.85$ and $\alpha = 6°$. The parameter varied is flight dynamic pressure.

of the damping coefficient at that particular dynamic pressure times the natural frequency of that mode. The ordinate is the imaginary part of the aeroelastic root, which is the frequency of the response of that mode at the dynamic pressure considered. Although one should note that the scales on the two axes are very different, it can be seen from the plot that the frequencies remained approximately unchanged throughout the whole range of dynamic pressures considered.

All the cases analyzed for this hammerhead shape were aeroelastically stable, although all the modes showed an initial tendency of going towards the unstable side for very small values of dynamic pressure. This tendency was quickly reversed as the dynamic pressure was increased further, such that it is hard to detect any of this behavior from the root locus plot for the first and second modes. For the third mode, however, the reversal of damping at low freestream dynamic pressure is clearly visible from Figure 9 . After this initial trend was passed, what we will call a *pure damping* behavior, for the lack of a better description, was observed. It is characterized by a simple increase of the damping in each mode as the flight dynamic pressure is raised. The frequencies remain approximately unchanged. This is not a typical aeroelastic behavior for conventional flight vehicle configurations with wings and tails. However, there are cases of one degree-of-freedom flutter. In other words, the fact that the frequencies remain approximately constant might just mean that this is one of such cases. It should also be noted that the natural frequencies considered for this analysis are quite high, which means that we are probably assigning stiffness values that are higher than they should be and explains why no flutter is observed. Moreover, since this configuration does not correspond to any existing vehicle, it is very difficult to try to correlate these results with some expected behavior.

The other hammerhead configuration considered reproduced the geometry of an Atlas-Able IV payload. The computational mesh about this vehicle was also generated by algebraic methods, and a three dimensional view of it can be seen in Figure 10. This grid also has $105 \times 66 \times 38$ points in the longitudinal, normal and circumferential directions, respectively. As in the previous applications, the circumferential direction has a periodic type mesh going 360° around the body. Appropriate grid stretching techniques were again used in order to optimize the distribution of the available computational mesh points. This configuration was studied at two different angles of attack, and both cases at $M_\infty = 0.85$. All computations used the turbulent flow option, and the Reynolds number based on the diameter of the afterbody cylindrical section was $Re = 1.2637 \times 10^6$.

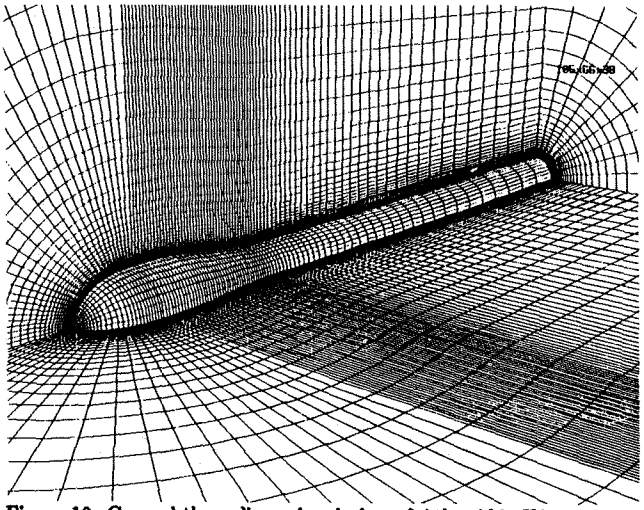

Figure 10: General three dimensional view of Atlas-Able IV computational mesh.

For the configuration at an angle of attack $\alpha = 6°$, an investigation of the sensitivity of the turbulence model with respect to the tuning of its computational parameters was performed. This investigation was motivated because some rather dramatic flow separation conditions were being observed in the computations. If we consider that the turbulence model used in the present calculations was originally derived for attached or mildly separated boundary layers, there is some reason for concern.

In the present implementation of the model, an important computational parameter is how far we search into the flowfield for the maximum velocity in the boundary layer profile. This distance is specified in terms of number of grid points in the normal direction from the wall. It was observed that some small variations in this parameter would cause large differences in the flow topology obtained.

Figure 11 shows oil-flow lines for the solution when this search was performed up to the 20th grid point. In this case there is a well-defined focus on the side of the body, as we can see from Figure 11(*a*). We can also identify a saddle point of separation on the lee generator just ahead of the ellipsoid-cylinder intersection (see Figure 11(*b*)). The release of particles around the focal point produces the particle traces plot shown in Figure 12. This figure shows how the particles are caught in the reversed flow region and are convected upstream, before reaching the forward flowing stream region. Details of the vortex "taking off" from the body surface can be seen in Figure 13, for the same particle trace plot shown in the previous figure. It is clear that the region of separated flow in the present case is very large. The complete boattail and most of the forebody cylindrical section are immersed in a reversed flow region.

If the search is performed up to the 25th grid point, a very different flow topology is obtained. The oil-flow lines in this case are shown in Figure 14. In this case there are two lines of separation over the side of the body. There is no focus anymore, and the critical point on the lee generator is not a saddle point but it is a node of separation. There is still an extensive region of separated flow but it is certainly smaller than in the previous case. Unrestricted particle traces for this solution can be seen in Figures 15 and 16. The former shows a side view of the body and the latter presents an expanded view of the flow separation

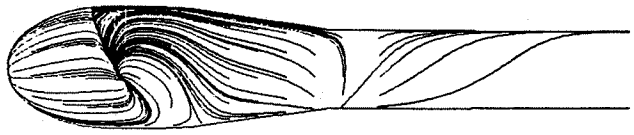

(*a*) Side view.

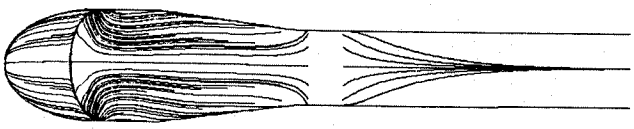

(*b*) Top view.

Figure 11: Oil-flow lines for Atlas-Able IV at $M_\infty = 0.85$ and $\alpha = 6°$ (computation with search up to 20th grid point).

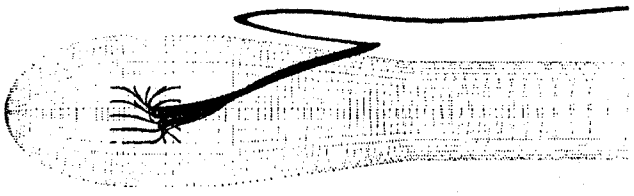

Figure 12: Side view of traces for particles released around the focal point on the side of the body.

Figure 13: Particle traces showing vortex leaving the body surface on the side of the vehicle.

around the leeside region.

If we keep increasing this distance of search, the trend continues in the sense that less separation is observed. For instance, Figure 17 shows a side view of the oil-flow lines obtained when the search is performed up to the 35th grid point. The flow on the forebody cylindrical section is fully attached in this case, and the separation region is limited to the "upper" portion of the boattail section. In terms of flow separation structure, the swirling of the flow around the focal point on the boattail is evident from the figure. It is also clear from this figure that the flow on the windside never separates, which is in contrast with the results previously shown for this configuration. Finally, when the search is performed up to the 45th grid point, the flow is fully attached as we can see in Figure 18.

The calculation with the search up to the 25th grid point seemed to produce the most realistic results in terms of flow topology, and it was adopted as the correct solution in this case. It must be said, however, that despite the dramatic differences in the flow topology, the calculated

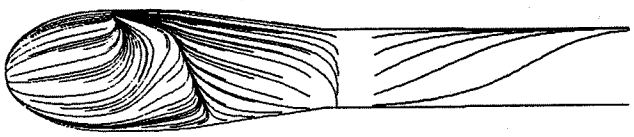

(*a*) Side view.

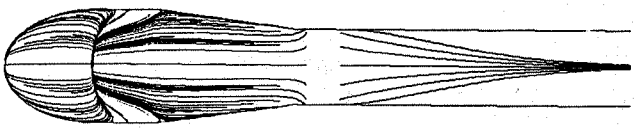

(*b*) Top view.

Figure 14: Oil-flow lines for Atlas-Able IV configuration at $M_\infty = 0.85$ and $\alpha = 6°$ (computation with search up to 25th grid point).

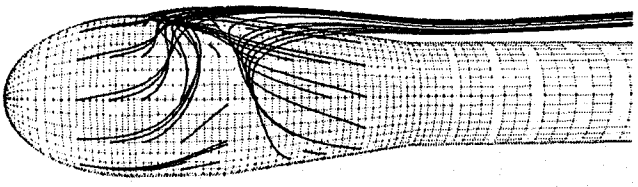

Figure 15: Particle traces showing flow separation on the Atlas-Able IV configuration at angle of attack (side view).

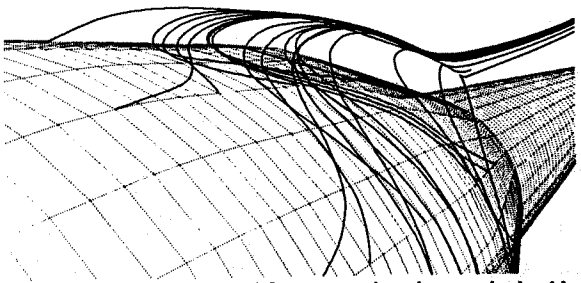

Figure 16: Expanded view of flow separation close to the leeside.

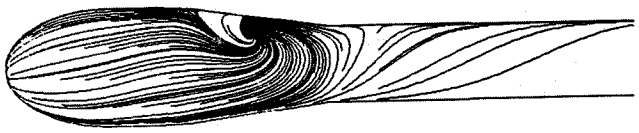

Figure 17: Side view of oil-flow lines for Atlas-Able IV configuration (computation with search up to 35th grid point).

Figure 18: Side view of oil-flow lines for Atlas-Able IV payload (computation with search up to 45th grid point).

pressures on the body did not present such large discrepancies among the various cases. To complement the visualization of the flowfield for this solution, Figure 19 presents a side view of the body where Mach number and density contours in the lee and wind planes are shown.

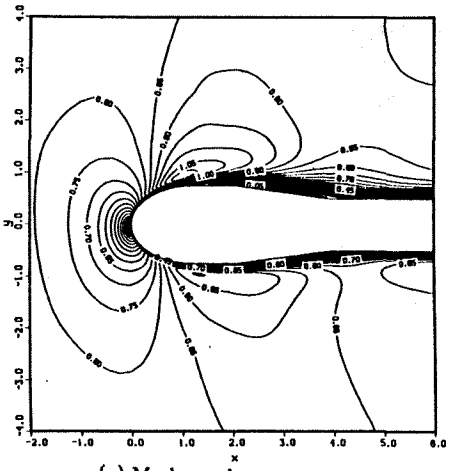

(a) Mach number contours.

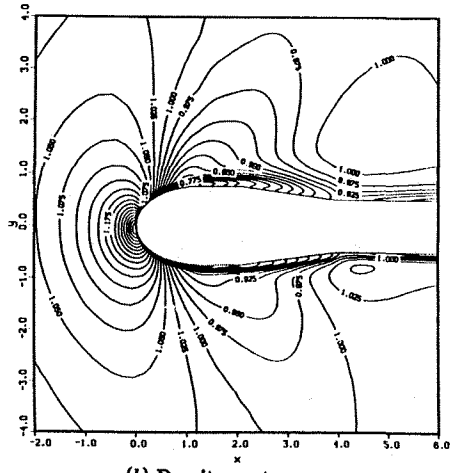

(b) Density contours.

Figure 19: Flow solution about an Atlas-Able IV configuration at $M_\infty = 0.85$ and $\alpha = 6°$ (side view).

This solution was used as an initial aerodynamic solution for the aeroelastic analysis of the present configuration. As in the previous case, this analysis was performed by varying the dynamic pressure while keeping the freestream Mach number and the angle of attack constants. A typical response obtained in this case is shown in Figure 20. An expanded view of the response in the second and third modes is shown in Figure 21. For this particular case, despite the very high flight dynamic pressure, the configuration is still aeroelastically stable. Three elastic modes were used in the analysis and we can see from the above figures that the oscillation in all three modes is being damped.

The results for the aeroelastic stability study of this configuration at $M_\infty = 0.85$ and $\alpha = 6°$ are summarized in Figure 22, which shows a plot of the modal damping coefficient as a function of the flight dynamic pressure. It was assumed that all modes had some amount of structural damping in this case. The damping in the first and third modes increases with the rise of the dynamic pressure. The second mode presented the most interesting behavior since there is a dynamic pressure range in which the damping decreases with the increase of the dynamic pressure.

This configuration was also studied at zero angle of attack and at the same flight Mach number $M_\infty = 0.85$. Only one aeroelastic run could be performed in this case due to the high computational cost of these aeroelastic solutions. The result indicated that the configuration was aeroelastically unstable at the dynamic pressure of 400 psf. More specifically, the second and third modes were showing a growing amplitude of oscillation. However, more cases at different values of dynamic pressure would have to be run in order to determine the actual flutter boundary. The results at $\alpha = 0°$ are discussed in more detail in Reference [10].

The results above reproduced the flight observations at least qualitatively since, according to results presented by Woods and Ericsson [22], the second mode was the one expected to go unstable. Unfortunately there was not enough experimental data on the structure properties in order to allow for a more quantitative comparison of these aeroelastic results. Nevertheless, the agreement obtained can already warrant some credibility to the method, although further validation is certainly necessary.

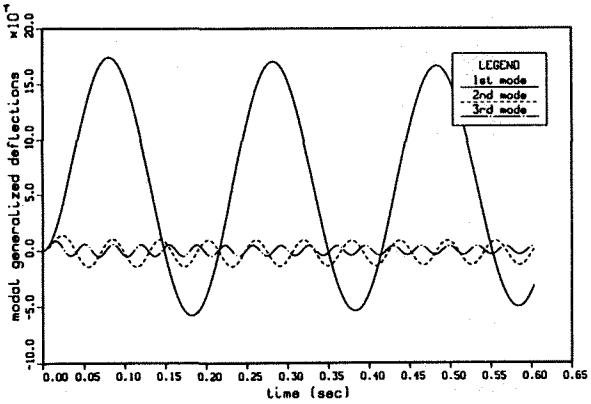


Figure 20: Modal response for Atlas-Able IV configuration at 1174 psf dynamic pressure ($M_\infty = 0.85$, $\alpha = 6°$).

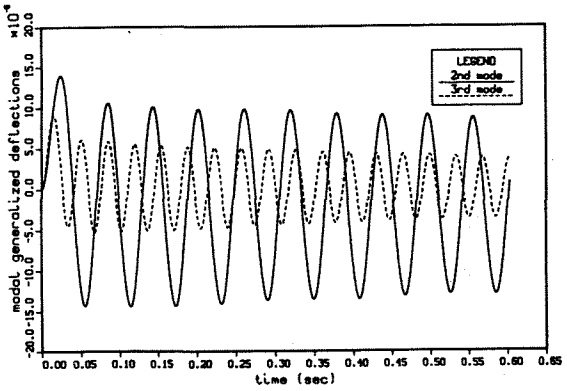


Figure 21: Expanded view of the response in the second and third modes for 1174 psf freestream dynamic pressure.

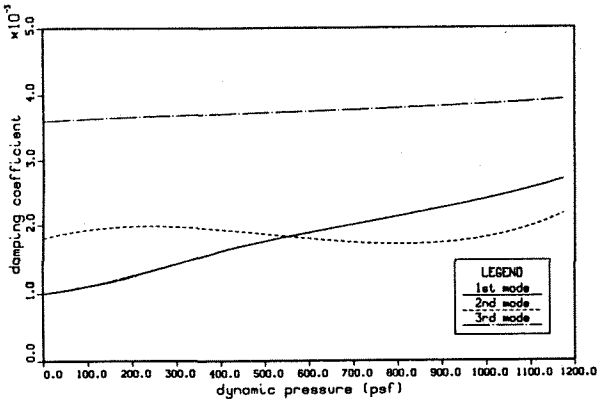


Figure 22: Influence of the airstream in the modal damping coefficient for an Atlas-Able IV payload at $M_\infty = 0.85$ and $\alpha = 6°$.

## Concluding Remarks

The formulation of the present method was described and considerations for its implementation were discussed. The results illustrate the application of the method for both steady and unsteady problems. The comparisons with the available steady state data provided a partial

validation of the method. It is well-recognized that unsteady data are difficult to find in the literature. This is very unfortunate because it would be very interesting to quantitatively compare our aeroelastic calculations. Nevertheless, as we saw in the previous section, the results are showing good qualitative agreement with the flight observations.

The results describing the uncertanties with respect to the correct flow topology and, therefore, with regard to the correct set of parameters for the turbulence model suggest that the present flow solver code may not be production-ready yet. Some difficulties with the present artificial dissipation algorithm, evidenced by results present in Reference [10], also confirm this suspicion. One should realize that the computation of such complex flowfields is not a trivial matter, and that the available numerical methods are just beginning to cope with such complexity. The advancement of our understanding of the phenomenon of turbulence and, in consequence, the improvement of its computational models should allow for more robust flowfield simulations for the kind of configurations and flight conditions we are interested in here. The continuous development of CFD methods is gradually allowing for consistent flow solutions without the need for *ad hoc* fixes.

A constant concern with these three dimensional simulations should be their computational cost. In the present case, the convergence to a steady state solution would typically take from 3500 to 4000 iterations considering that one started from scratch, i. e. , assuming freestream everywhere. This does not constitute too much CPU time in the hemisphere-cylinder cases since the grid was small. For the hammerhead payload configurations, however, a more realistic grid was used and each steady state iteration would take approximately 10 CPU seconds in a CDC Cyber 205. Therefore, something of the order of 10 CPU hours were being necessary to achieve convergence in this case. On the other hand, it is important to point out that once a converged solution has been obtained for a certain flight condition, it could be used as the initial field solution for the computations at a different flight condition. This can result in considerable cost savings.

For the grid size used in the hammerhead cases, each aeroelastic iteration takes approximately 12 CPU seconds. A response solution as shown in Figure 20 takes approximately 9 CPU hours in the Cyber 205. One should note that only three cycles of the lowest mode were calculated in that case. The important conclusion is that the high computational costs are still preventing a more detailed parametric study of the flutter boundaries for these complex configurations. The author believes that such high costs can be perfectly justified in a research effort, but they will certainly have to be brought down before the industry could accept the method as a valid analysis tool. It must be said, however, that the enormous development in hardware capabilities we are currently witnessing will make the computational requirements of the present method seem very modest in just a few years, even if no improvement is made to the current algorithms.

## Acknowledgments

This research was partially supported by the Brazilian Government under a scholarship provided by Instituto de Atividades Espaciais, and partially supported by the National Aeronautics and Space Administration under Grant NGL-05-020-243. It was performed while the author was a graduate student at Stanford University.

## References

[1] MacCormack, R.W., "Numerical Computation of Viscous Flow," Notes for course AA214C, Dept. of Aeronautics and Astronautics, Stanford University, Stanford, CA, April-June 1986.

[2] Anderson, D.A., Tannehill, J.C., and Pletcher, R.H., *Computational Fluid Mechanics and Heat Transfer*, McGraw-Hill, New York, 1984.

[3] Warming, R.F., "Topics in Computational Fluid Dynamics," Notes for course AA215A, Dept. of Aeronautics and Astronautics, Stanford University, Stanford, CA, January-March 1984.

[4] Pulliam, T.H., and Steger, J.L., "Implicit Finite-Difference Simulations of Three-Dimensional Compressible Flow," *AIAA Journal*, Vol. 18, No. 2, Feb. 1980, pp. 159-167.

[5] Hinze, J.O., *Turbulence*, 2nd Edition, McGraw-Hill, New York, 1975.

[6] Baldwin, B.S., and Lomax, H., "Thin Layer Approximation and Algebraic Model for Separated Turbulent Flows," AIAA Paper No. 78-257, January 1978.

[7] Beam, R.M., and Warming, R.F., "An Implicit Finite-Difference Algorithm for Hyperbolic Systems in Conservation-Law Form," *Journal of Computational Physics*, Vol. 22, 1976, pp. 87-110.

[8] Beam, R.M., and Warming, R.F., "An Implicit Factored Scheme for the Compressible Navier-Stokes Equations," *AIAA Journal*, Vol. 16, No. 4, April 1978, pp. 393-402.

[9] Pulliam, T.H., and Steger, J.L., "Recent Improvements in Efficiency, Accuracy and Convergence for Implicit Approximate Factorization Algorithms," AIAA Paper 85-0360, *AIAA 23rd Aerospace Sciences Meeting*, Reno, Nevada, January 1985.

[10] Azevedo, J.L.F., "Transonic Aeroelastic Analysis of Launch Vehicle Configurations," PhD Thesis, Dept. of Aeronautics and Astronautics, Stanford University, Stanford, CA, Feb. 1988.

[11] Azevedo, J.L.F., "Aeroelastic Analysis of Launch Vehicles in Transonic Flight," AIAA Paper No. 87-0708-CP, *28th AIAA/ASME/ASCE/AHS Structures, Structural Dynamics and Materials Conference*, Monterey, CA, April 1987.

[12] Deiwert, G.S., and Rothmund, H., "Three-Dimensional Flow Over a Conical Afterbody Containing a Centered Propulsive Jet: A Numerical Simulation," AIAA Paper 83-1709, *AIAA 16th Fluid and Plasma Dynamics Conference*, Danvers, Mass. , July 1983.

[13] Ying, S.X., Steger, J.L., Schiff, L.B., and Baganoff, D., "Numerical Simulation of Unsteady, Viscous, High-Angle-of-Attack Flows Using a Partially Flux-Split Algorithm," AIAA Paper 86-2179, *AIAA 18th Atmospheric Flight Mechanics Conference*, Williamsburg, Virginia, August 18-20, 1986.

[14] Ying, S.X., "Three-Dimensional Implicit Approximately Factored Schemes for the Equations of Gasdynamics," SUDAAR No. 557, Dept. of Aeronautics and Astronautics, Stanford University, Stanford, CA, June 1986.

[15] Liepmann, H.W., and Roshko, A., *Elements of Gasdynamics*, John Wiley & Sons, New York, 1957.

[16] Hsieh, T., "An Investigation of Separated Flows About a Hemisphere-Cylinder at Incidence in the Mach Number Range from 0.6 to 1.5," AIAA Paper 77-179, *AIAA 15th Aerospace Sciences Meeting*, Los Angeles, CA, January 1977.

[17] Hsieh, T., "Low Supersonic Flow over Hemisphere-Cylinder at Incidence," *Journal of Spacecraft and Rockets*, Vol. 14, No. 11, Nov. 1977, pp. 662-668.

[18] Dallmann, U., "Topological Structures of Three-Dimensional Flow Separations," DFVLR Report No. 221-82 A 07, April 1983.

[19] Dallmann, U., "Topological Structures of Three-Dimensional Vortex Flow Separation," AIAA Paper No. 83-1735, *AIAA 16th Fluid and Plasma Dynamics Conference*, Danvers, Mass. , July 1983.

[20] Kaynak, Ü. , Holst, T.L., and Cantwell, B.J., "Computation of Transonic Separated Wing Flows Using an Euler/Navier-Stokes Zonal Approach," NASA TM 88311, July 1986.

[21] Deiwert, G.S., "Topological Analysis of Computed Three-Dimensional Viscous Flow Fields," in *Recent Contributions to Fluid Mechanics*, W. Haase, ed. , Springer-Verlag, New York, 1982, pp. 40-49.

[22] Woods, P., and Ericsson, L.E., "Aeroelastic Considerations in a Slender, Blunt-Nose, Multistage Rocket," *Aerospace Engineering*, Vol. 21, No. 5, May 1962, pp. 42-51.